Performance evaluation of the **LightPath** imaging system for intra-operative Cerenkov luminescence imaging

Esther Ciarrocchi (esther.ciarrocchi@df.unipi.it)[a,*], Christian Vanhove (christian.vanhove@ugent.be)[b], Benedicte Descamps (benedicte.descamps@ugent.be)[b], Stef De Lombaerde (stef.delombaerde@ugent.be)[c], Stefaan Vandenberghe (stefaan.vandenberghe@ugent.be)[b], Nicola Belcari (nicola.belcari@unipi.it)[a]

[a] *University of Pisa, Department of Physics, Largo Bruno Pontecorvo 3, Pisa, Italy, 56127*
[b] *University of Ghent, IBiTech-MEDISIP, C. Heymanslaan 10, Ghent, Belgium, B-9000*
[c] *University of Ghent, Faculty of Pharmaceutical Sciences Laboratory of Radiopharmacy, Ottergemsesteenweg 460, Ghent, Belgium, B-9000*

Abstract

In this study, the performances of an intra-operative optical imaging system for Cerenkov luminescence imaging of resected tumor specimens were evaluated **with phantom studies**. The spatial resolution, the linearity of the measured signal with the activity concentration and the minimum detectable activity concentration were considered. A high linearity was observed over a broad range of activity concentration ($R^2 \geq 0.99$ down to $\sim$40 kBq/ml of ^{18}F-FDG). For ^{18}F-FDG activity distributions 2 mm deep in biological tissue, the measured detection limit was 8 kBq/ml and a spatial resolution of 2.5 mm was obtained. **The detection limit of the imaging system is comparable with clinical activity concentrations in tumor specimens, and the spatial resolution is compatible with clinical requirements.**

Keywords: Cerenkov luminescence imaging, intra-operative imaging, performance evaluation, beta-emitting radiotracer

*Corresponding author

Introduction

Surgery is the cornerstone of the treatment of many solid localized tumors, but its effectiveness is highly dependent on the extent and radicality of the excision, as a compromise between the complete resection of the cancer and the conservation of the healthy surrounding tissue to limit the functional damage to the organ. Currently, tumor margins are identified with frozen section procedure which needs to be confirmed by a post-operative histology of the resected specimen, resulting in a lengthy and costly procedure.

Cerenkov luminescence imaging (CLI) is an optical imaging modality in which a β-emitting radiotracer is imaged by means of the Cerenkov luminescence produced in biological tissue [1, 2, 3]. Cerenkov luminescence is blue-white visible light produced by charged particles traveling in a dielectric medium with a velocity greater than the phase velocity of light in the medium. The Cerenkov effect produces a small signal (1-100 photons per decay) with a few mm penetration depth in tissue, but the light emission is highly localized around the radiotracer distribution [4, 5].

CLI can be helpful intra-operatively in assessing tumor margins after the patient has been injected a radiotracer [6]. Once the tumor has been surgically resected, it is imaged in real time to determine whether its margins are luminescent (i.e., belonging to the tumor) or not (i.e., healthy tissue has been reached). Intra-operative CLI can be performed with already approved PET tracers, therefore avoiding the regulatory hurdles of fluorescence-guided surgery.

The applicability of CLI to guided surgery had already been proposed when CLI was introduced [7], and the feasibility *in-vivo* had been demonstrated using a fiber-based Cerenkov endoscopy system on phantoms and mouse models [8]. A detailed review of the first studies of CLI image-guided surgery can be found in Ref. [6]. More recently, the investigation has expanded to the clinical field. CLI images have been acquired in neurosurgery [9] and in breast-conserving surgery [10]. The potential application to brain tumor radio-guided resection has been further investigated with Monte Carlo simulations [11].

The goal of this study was to evaluate the spatial resolution, sensitivity to activity concentration and linearity of the LightPath™ (Lightpoint Medical, Ltd, UK) imaging system for intra-operative CLI, in conditions that were reproducible and similar to the clinical situation. The system is technologically similar to other commercial optical imagers, featuring a sensitive photodetector placed in a light-tight container. The difference with other commercial systems, which are mainly dedicated to preclinical applications, is the CE-mark approval which allows a straight-forward use in clinical observational studies, also by positioning the system directly inside the operative theater. ^{18}F-FDG was used for all the measurements, not only because ^{18}F is the radioisotope producing the smallest number of Cerenkov photons, thus representing the worst case scenario, but also because it is the most often used PET radiotracer in clinical practice due to its wide applicability. **Even if the setups chosen for the performance evaluation do not reproduce exactly the clinical scenario, the measurements can be easily repeated with different imaging systems for performance comparison.**

1. Materials and Methods

1.1. Imaging system and acquisition settings

The LightPath™ imaging system has been specifically developed to aid in tumor margin delineation by detecting the Cerenkov luminescence produced by a β-emitting radio-tracer. It is a device featuring a light-tight imaging chamber for the specimen placement, an electron-multiplying charge coupled device (EMCCD) camera for the CLI acquisition, a white-light reference camera for photographic images, a mirror assembly to switch between the two cameras and an integrated computer to control the imaging system [6]. The reference camera has 1600×1200 pixels and is coupled with a f/1.4 lens to capture images illuminated by four banks of LEDs at 45° with respect to the specimen plane. The EMCCD (Andor iXon Ultra 897) is Peltier cooled to -80° C and it is fitted

with a f/0.95, 50 mm focal length lens. The camera has 512 × 512 pixels (with 16 μm pixel size) and works at a fixed distance, with a 60 mm field of view. The depth of field of the CLI system is up to 30 mm above the specimen holder surface. To increase sensitivity, the EM gain of the camera is fixed to 300 and the gain of the output preamplifier is set to 3.

The manufacturer declared the following nominal performances: the detection limit, determined as the signal giving a ratio of one when dividing the camera noise, is 2.64 kBq/ml for 200 μl of clear Fluorine-18 solution in 300 μl Eppendorf tubes, measured using five minutes exposure time and 8×8 binning factor. The nominal linearity is r=0.9998 up to 1.8 MBq/ml of Fluorine-18 solution (4.5 ml) in a 50 mm petri dish, measured using 60 s exposures with 2×2 pixel binning factor.

The system applies a 3 × 3 pixels median filter mask to the image to filter out direct detection of high energy photons (e.g. gamma radiation, annihilation photons, cosmic rays). If a series of images was acquired, also a temporal median filter is applied. The correction is applied only to pixels whose value is above 5% of the maximum pixel value in the image. An additional Gaussian filter (σ = 3 pixels, threshold of 50% of maximum value) further smooths the median-filtered image. The image is then rotated, translated and interpolated to align with the reference image (1600×1200 pixels).

In this study, images were acquired with settings that could increase the detection capability while maintaining exposure times compatible with real clinical applications. **It was verified with a preliminary acquisition that by increasing the pixel binning factor from 1 to 8, the spatial resolution worsened by less than 30%, but an 8-fold increase in the peak-to-noise ratio could be obtained.** Therefore, pixel binning factor 8×8 was employed, and exposure times of 5 minutes or less were used.

1.2. Intrinsic spatial resolution

The *intrinsic* system spatial resolution was determined with an edge spread function (ESF) measurement, obtained by diluting in a Petri dish ^{18}F-FDG

with a mixture of water and fat emulsion and by covering half of the Petri dish with black tape. Three images were acquired to estimate the uncertainty of the measurement, and one is shown in Fig. 1(a) as an example. Hot spots, due to the direct detection of high energy photons, are visible and were excluded in the image processing.

To determine spatial resolution, a rectangular region of interest (ROI) was selected across the edge (as indicated in the image), and the edge profiles in this region were averaged to obtain the mean edge profile. The LSF was determined as the derivative of this mean ESF and its FWHM was calculated to estimate the system spatial resolution.

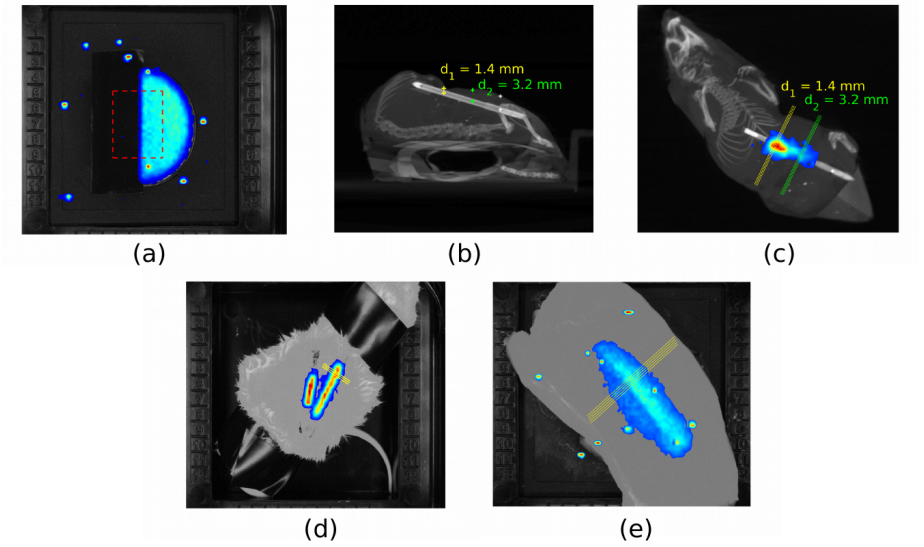

Figure 1: (a) Representative CLI image of the ESF, used to determine the intrinsic spatial resolution of the imaging system. Hot spots due to the direct detection of high energy photons are visible and were discarded in the image processing. (b) Sagittal CT view of mouse-IP in supine position (from the paws point of view); the capillary tube, the spine and the mouse support are visible. (c) CLI image of the LSF in the mouse-IP, superimposed on the top view of the CT image; the selected profiles used to evaluate spatial resolution at different depths are indicated. (d) Image of the LSF in the mouse-SC, used in the estimation of the effective spatial resolution in tissue. The animal head is in the top-right corner. (e) Representative image of the LSF in chicken breast, used to determine the effective spatial resolution, at depth $d = 12$ mm.

1.3. Effective spatial resolution in tissue

For this measurement, ^{18}F-FDG was diluted in water and injected into glass capillary tubes of $d_O = 1.55 \pm 0.05$ mm outer diameter. The capillary tubes were placed in the abdomen of a *post-mortem* mouse model (n = 2 Balb/C mice): (1) subcutaneously, parallel to the mouse skin, (2) deeper in the abdominal cavity, oblique with respect to the abdomen surface in order to provide different source depths for a fixed activity concentration. In the remainder of this paper, we will refer to these two settings as *mouse-SC* (subcutaneous source) and *mouse-IP* (intraperitoneal source), respectively. For the mouse-IP, the location of the line source was estimated through a CT scan (obtained with a Small Animal Radiation Research Platform, SARRP, XStrahl, Surrey, UK). A sagittal CT view of mouse-IP in supine position is shown in Fig. 1(b), while a top view of the animal is reported in Fig. 1(c), with the CLI image in false color scale. The selected profiles at two depths are indicated. The source depth ($d = 1.4$ mm in yellow, $d = 4$ mm in green) was estimated by means of the CT acquisition. For the mouse-SC, the source depth was estimated to be 500 μm, approximately corresponding to the skin thickness. A representative image of two line sources in the mouse-SC is shown in Fig. 1(d). The region where the line source profiles were selected is also shown. To investigate greater source depths, the same test was performed placing the line source under slabs of chicken breast of different thickness. A CLI image of the line source at a depth of 12 mm is shown in Fig. 1(e), along with the selected profiles.

To determine the spatial resolution, several line source profiles were selected, and the spatial resolution (Res) was determined by subtracting in quadrature the nominal outer diameter of the line source (OD) from the full width at half maximum (FWHM) of the source profile ($\text{Res} = \sqrt{\text{FWHM}^2 - \text{OD}^2}$).

1.4. Linearity

To verify the proportionality of the measured signal to the activity level at the time of the measurement, series of images were acquired over a few hours. This was done with the ^{18}F-FDG line source in the mouse-SC, Fig. 2(a), over a

large range of activity levels (2 half-lives), and with one ^{18}F-FDG-agar phantom covered by a slab of tissue at smaller activities (Fig. 2(b), more details on this kind of specimen are provided in 1.5).

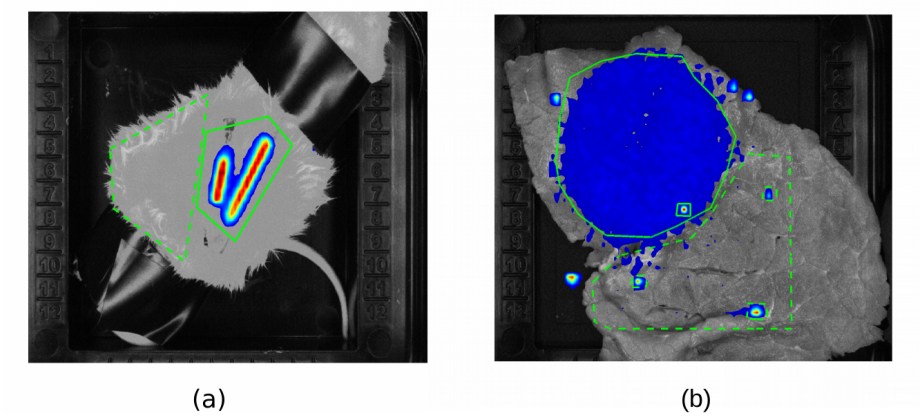

Figure 2: (a) Selected ROIs for linearity evaluation in the mouse-SC. (b) Sample image of the ^{18}F-FDG-agar phantom under a 2 mm thick slab of bovine tissue. The ROIs involved in the linearity and detection limit evaluation, with the excluded hot pixels, are also indicated.

Two ROIs were selected in the images: ROI_S was the region containing the image of the source (continuous contour), while ROI_B was a background region (dashed contour). Hot spots were excluded in both regions, as shown in Fig. 2(b). In addition, the background region ROI_B was chosen where tissue was present to account for any possible tissue auto-luminescence phenomena. The signal $(\mu_S - \mu_B)$ was calculated, and its correlation with the activity concentration (in the line source and in the agar phantom, respectively) at the time of the acquisition was determined through a linear fit. The adjusted coefficient of determination R^2 [12] was used as metric for the linearity evaluation.

1.5. Detection limit

The system detection limit, i.e. the minimum detectable activity concentration, was evaluated using the ^{18}F-FDG-agar phantoms covered by a slab of beef meat of approximately 2 mm thickness, Fig. 2(b). The reason for such phantoms was to reproduce the realistic situation of a radio-labeled volume surrounded

by healthy tissue. Agar was chosen because it allows to obtain semi-solid phantoms with uniform activity distribution and which can be easily shaped [13]. The ^{18}F-FDG-agar phantoms were placed under a tissue slab to account for the attenuation of light by biological tissue. Red meat was chosen due to the large presence of (highly absorbing) hemoglobin. To obtain the phantoms, 400 mg of agar powder were mixed to 20 ml of distilled water, a small amount ($\sim$ 100 μl) of ^{18}F-FDG was added, and the mixture was warmed up and mixed with a magnetic stirring bar for a few minutes. When it appeared clear, the compound was poured in Petri dishes, covered and put in the fridge for approximately one hour to solidify. The phantoms were shaped using molds, and volumes as those shown in Fig. 3(a) were obtained.

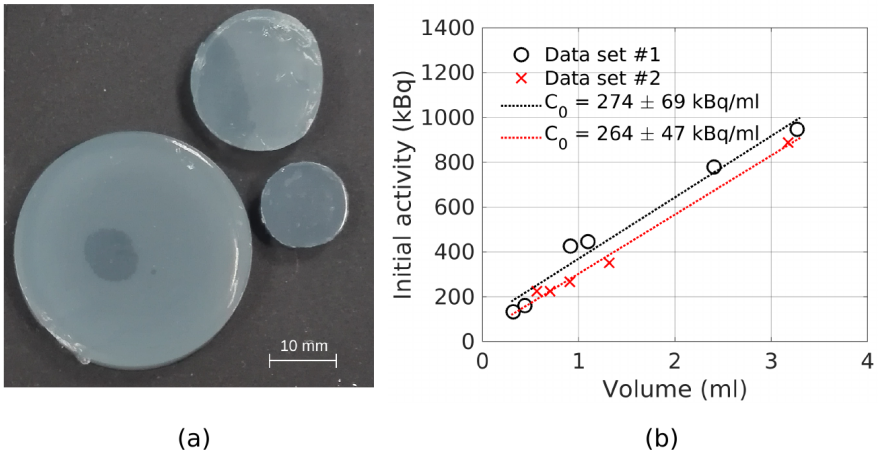

Figure 3: (a) Representative set of ^{18}F-FDG-agar phantoms used for detection limit measurements. (b) Correlation between the phantom volume and the ^{18}F activity, for the two phantom sets. The dashed lines show the estimated activity concentration in the two phantom sets, obtained with a linear fit.

Two sets of phantoms were prepared for this study, and the activity and the dimensions of each were measured. In addition, a CT acquisition was used to verify the absence of air bubbles in the volumes. Although only two phantoms were used in the detection limit evaluation, the two full sets were used to validate the activity measurement performed with the dose calibrator. In fact, with this preparation method, phantoms belonging to the same set should have the same

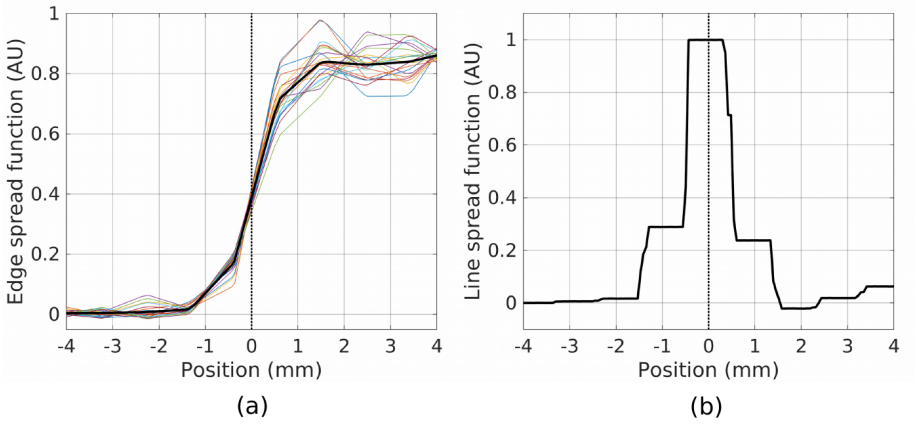

Figure 4: Intrinsic spatial resolution determination using the ESF. (a) Set of edge spread functions and mean ESF, (b) line spread function, for the image shown in Fig. 1(a).

activity concentration. Figure 3(b) reports the dependence of the measured phantom activity on its volume, for the two phantom sets. As can be seen, a uniform activity concentration C_0 was obtained by means of a linear fit, with a 25% and 18% uncertainty in the two sets, respectively.

The detection limit of the imaging system was determined as the activity concentration (in kBq/ml) providing a signal ($\mu_S - \mu_B$) equal to the noise in the image (σ_B), calculated in the ROIs indicated in Fig. 2(b).

2. Results and Discussion

2.1. Intrinsic spatial resolution

Figure 4(a) shows a set of ESF profiles in the selected ROI and the obtained mean ESF, for the image shown in Fig. 1(a). The LSF derived from the ESF is shown in Fig. 4(b). A spatial resolution of 0.98 ± 0.06 mm FWHM was obtained, dominated by the pixel binning factor contribution. The uncertainty on the obtained value corresponds to the pixel size of the interpolated image returned by the software.

It was verified that, by using the raw uncorrected images, the intrinsic spatial resolution corresponds to the pixel binning factor contribution (FWHM =

0.9375 mm). The difference between the two resolution values is due to the image correction algorithm (median and Gaussian filters). However, the resolution of the final corrected image is only slightly larger than the resolution of the raw image, which is included in its uncertainty (0.06 mm). Therefore, the degradation of the spatial resolution due to the image correction algorithm is negligible.

2.2. Effective spatial resolution in tissue

Figure 5(a) shows a set of representative LSF profiles in the mouse models and in chicken breast. The amplitude is normalized to the maximum of each curve, while the shape and width depends on the source depth and on the type of tissue. Figure 5(b) summarizes the measured spatial resolution (in mm FWHM) for the line source at different depths in the mouse models and in chicken breast. The spatial resolution worsens significantly as the radioactive distribution is placed deeper in the tissue, with a strong degradation for sources deeper than 5 mm in tissue. However, in clinical applications it will be most likely to image a radioactive distribution a few mm deep in tissue, and in those cases a spatial resolution of less than 5 mm was observed. **As reported in [14], the spatial resolution can potentially be improved by combining several planar images acquired with different emission filters. The LightPath imaging system currently features a filter wheel with two short-pass filters with cutoff wavelengths of 550 and 800 nm, to filter out longer wavelengths produced deeper in the specimen, and two spare locations. In the future development of the LightPath system, it might be interesting to study the increase in resolution achievable by inserting appropriate narrow band-pass filters and combining the spectral images.**

2.3. Linearity

Figure 6(a) shows the CLI measured count rate ($\mu_S - \mu_B$, divided by the exposure time) as a function of the activity concentration at the time of the

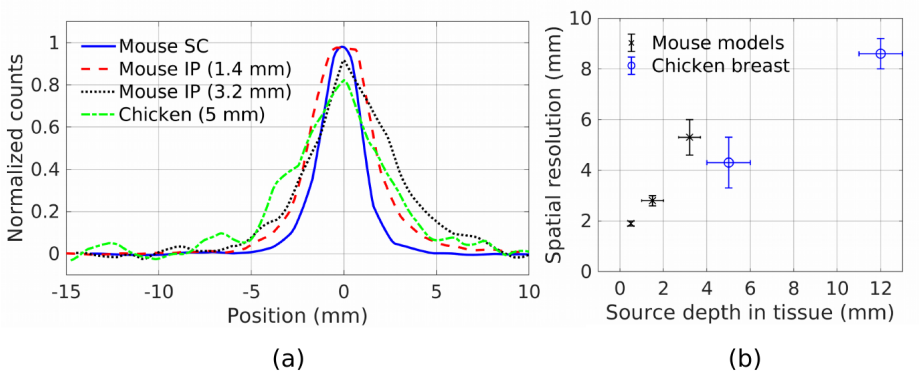

Figure 5: (a) Representative set of LSF profiles in different tissue types. (b) Calculated spatial resolution in tissue, for different types and source depths.

acquisition, for the line source in the mouse-SC. The linear fit and the corresponding coefficient of determination show a high correlation between the two quantities. Figure 6(b) shows the results at lower activity concentrations in the agar phantom. It should be noted that in this case the linear relation between the two quantities is different (i.e., different p_i) because the CLI signal depends on the optical properties and geometry of the specimen.

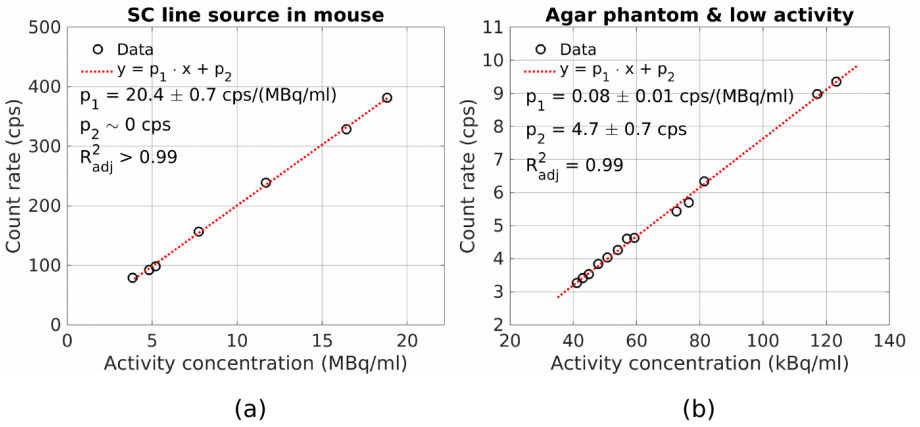

Figure 6: Linearity of the CLI signal with activity concentration: (a) in the line source for the mouse-SC case, (b) in the agar phantom for low concentrations.

The linearity of the Cerenkov signal with the activity concentration has been demonstrated by many studies, also in terms of correlation of the Cerenkov and

PET signals [6]. These studies mainly imaged water solutions of radio-tracers with an IVIS imaging system, see for example [2, 15, 16]. The proportionality of the number of detected photons with the activity concentration in water solution has been verified also using digital silicon photo-multipliers as photo-detectors [17], and when amplifying the CLI signal by means of a liquid scintillator [18]. In biological tissue, Cerenkov photons are attenuated more than in water, but also in this case a correlation between the number of photons and the activity concentration is expected. In Ref. [19], the proportionality between the CLI radiance and the activity concentration in a tumor mouse model was demonstrated. In this study, the linearity in tissue was verified also for the specific imaging system used and at various activity levels.

2.4. Detection limit

Figure 7(a) reports the mean count rate in the source and background regions (circles and diamonds, respectively) as a function of the activity concentration in the specimen at the time of the measurement for the first data set. The standard deviations in the two regions are shown on the right (Fig. 7(b), triangles for the source and crosses for the background). Figure 7(c) shows the measured signal (blue squares) as a function of the activity concentration and its linear fit (blue solid line), extrapolated to low concentrations (blue dotted line). The image noise (red crosses) and its extrapolation (red dashed line) are also reported. The results for the second data-set are indicated in green.

Based on this plot, the detection limit of the system was approximately 8 kBq/ml, a factor 3 larger than the nominal value in air declared by the manufacturer (2.64 kBq/ml for pure radioisotope). In order to have an activity concentration in the tumor specimen equal to 8 kBq/ml, a patient should be injected 11 MBq/kg roughly an hour before imaging, if the injected ^{18}F-FDG would distribute uniformly inside the human body (assuming water density). However, tumor regions exhibit an increased uptake compared to healthy tissue, featuring a standardized uptake value (SUV) typically ranging from 3 to 12 [20]. Therefore, this activity concentration in a tumor region can be ob-

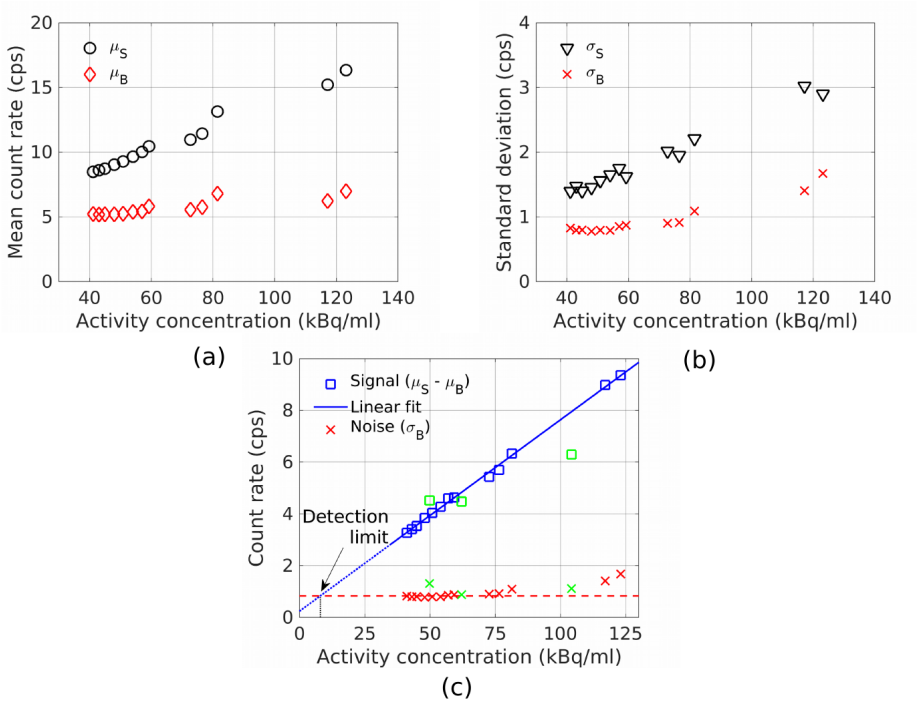

Figure 7: Detection limit estimation for the ^{18}F-FDG-agar phantom under a 2 mm thick slab of bovine tissue. (a) Mean count rate in a source (black circles) and background (red diamonds) region as a function of the activity concentration in the specimen at the time of the measurement, for the first data set. (b) Standard deviation of count rate in a source (black triangles) and background (red crosses) region as a function of the activity concentration, for the first data set. (c) Measured signal ($\mu_S - \mu_B$, blue squares) as a function of the activity concentration, linear fit of the signal (blue solid line), extrapolated to low concentrations (blue dotted line). The image noise (red crosses) and its extrapolation (red dashed line) are also reported. The results for the second data-set are shown in green.

tained even with smaller doses. Since 3-10 MBq/kg of ^{18}F-FDG are typically injected for a PET examination [6, 21], this effective detection limit in tissue is still compatible with clinical requirements. Furthermore, for more superficial sources the detectable signal for a given activity concentration will be higher, thus we can expect the system to be able to detect even lower concentrations. Lastly, the detection capability could be improved also by using radioisotopes with much higher CLI efficiency. For example, an increase by a factor $\sim$17 is expected in the number of Cerenkov photons produced in tissue ($n = 1.4$) by employing ^{68}Ga instead of ^{18}F [16, 22], **whilst a concentration in a brain tumor specimen of 4.8 kBq/ml could be detected with ^{90}Y [9], a radioisotope producing in tissue 23 times more Cerenkov photons than ^{18}F.** The first clinical CLI observational studies have indicated that an oral administration of 550 MBq of ^{131}I allowed to image after 24 hours a thyroid gland of a patient with hyperthyroidism [23], and that lymph nodes located 16 mm under the skin and with activity concentration as low as 30 kBq/ml were detected [24]. A direct comparison of our measured detection limit with the results of these studies would require additional information to model the Cerenkov photons transport, taking into account the different source depth, light attenuation, and detection geometry in the three cases. However, the fact that our measured detection limit is compatible with clinical procedures along with these first in-human results seem promising for the application of CLI in radio-guided surgery.

Conclusions

The spatial resolution, linearity, and detection limit of the **LightPath** imaging system for intra-operative CLI were evaluated **with phantom studies**. ^{18}F was used because it is the radioisotope with the least Cerenkov light production, thus being more suitable to test the performance in the worst case scenario. A spatial resolution of less than 5 mm was measured for superficial sources (less than 5 mm deep in tissue). The response of the imaging system was found linear

over a broad range of activity concentrations. A detection limit of ∼8 kBq/ml was estimated for a radioactive distribution 2 mm deep in tissue. **The spatial resolution, measured in the chosen reproducible setups, is compatible with the requirements of image-guided surgery and the sensitivity of the imaging system is of the order of clinical activity concentrations in resected tumor specimens.**

In this study, the activity distribution extension and position was known a priori. However, before the clinical application of CLI to the intra-operative contest, the margin assessment capability will need to be validated with a histological examination of the specimens. Another critical aspect is understanding the actual potential utility of intra-operative CLI in comparison to PET imaging of the tumor specimens. In fact, while it is true that CLI is a rapid imaging tool, relatively cost-effective, portable and with reasonable spatial resolution, it provides a two-dimensional image. A high spatial resolution PET scanner (like a preclinical one) could potentially be sensitive to lower activities and sufficiently accurate for clinical needs, having also the advantage of providing a three-dimensional view of the specimen. In addition, it would be interesting to compare the performance of different optical imaging systems by reproducing the results of this study, **to evaluate the impact of using a fiber-optic system around the tumor specimen, as suggested in [25] for small animal imaging**, and also of employing different PET tracers **or β^- emitters. In this last case, it would be useful to determine the advantages of intra-operative CLI with respect to radio-guided surgery by direct detection of the β particle, as done in [26].**

Disclosure

The authors declare that they have no relevant financial interests in the manuscript and no other potential conflicts of interest to disclose. In this study, only *post-mortem* animal models that had already been sacrificed were used. Institutional policies at the University of Gent do not require any formal approval

in this case.

Funding sources

This research was partially supported by the FOE research grant provided by the Italian Ministry of Education, University and Research (MIUR) to the Euro-BioImaging Multi-modal Molecular Imaging Italian Node.

References

[1] R. Robertson, M. Germanos, C. Li, G. Mitchell, S. Cherry, M. Silva, Optical imaging of Cerenkov light generation from positron-emitting radiotracers, Physics in Medicine and Biology 54 (16) (2009) N355.

[2] A. Ruggiero, J. Holland, J. Lewis, J. Grimm, Cerenkov luminescence imaging of medical isotopes, Journal of Nuclear Medicine 51 (7) (2010) 1123–1130.

[3] A. Spinelli, D. D'Ambrosio, L. Calderan, M. Marengo, A. Sbarbati, F. Boschi, Cerenkov radiation allows in vivo optical imaging of positron emitting radiotracers, Physics in Medicine and Biology 55 (2) (2010) 483.

[4] A. Spinelli, F. Boschi, Novel biomedical applications of Cerenkov radiation and radioluminescence imaging, Physica Medica 31 (2) (2015) 120–129.

[5] E. Ciarrocchi, N. Belcari, Cerenkov luminescence imaging: physics principles and potential applications in biomedical sciences, EJNMMI physics 4 (1) (2017) 14.

[6] M. Grootendorst, M. Cariati, A. Kothari, D. Tuch, A. Purushotham, Cerenkov luminescence imaging (CLI) for image-guided cancer surgery, Clinical and Translational Imaging 4 (5) (2016) 353–366.

[7] J. Holland, G. Normand, A. Ruggiero, J. Lewis, J. Grimm, Intraoperative imaging of positron emission tomographic radiotracers using Cerenkov luminescence emissions, Molecular Imaging 10 (3) (2011) 177.

[8] H. Liu, C. Carpenter, H. Jiang, G. Pratx, C. Sun, M. Buchin, S. Gambhir, L. Xing, Z. Cheng, Intraoperative imaging of tumors using Cerenkov luminescence endoscopy: a feasibility experimental study, Journal of Nuclear Medicine 53 (10) (2012) 1579–1584.

[9] A. Spinelli, M. Schiariti, C. Grana, M. Ferrari, M. Cremonesi, F. Boschi, Cerenkov and radioluminescence imaging of brain tumor specimens during neurosurgery, Journal of Biomedical Optics 21 (5) (2016) 050502–050502.

[10] M. Grootendorst, M. Cariati, S. Pinder, A. Kothari, M. Douek, T. Kovacs, H. Hamed, A. Pawa, F. Nimmo, J. Owen, et al., Intraoperative Assessment of Tumor Resection Margins in Breast-Conserving Surgery Using 18F-FDG Cerenkov Luminescence Imaging: A First-in-Human Feasibility Study, Journal of Nuclear Medicine 58 (6) (2017) 891–898.

[11] J. Klein, G. Mitchell, S. Cherry, Quantitative assessment of Cerenkov luminescence for radioguided brain tumor resection surgery, Physics in Medicine and Biology 62 (10) (2017) 4183.

[12] A. K. Srivastava, V. K. Srivastava, A. Ullah, The coefficient of determination and its adjusted version in linear regression models, Econometric reviews 14 (2) (1995) 229–240.

[13] B. Pogue, M. Patterson, Review of tissue simulating phantoms for optical spectroscopy, imaging and dosimetry, Journal of Biomedical Optics 11 (4) (2006) 041102–041102.

[14] A. Spinelli, C. Kuo, B. Rice, R. Calandrino, P. Marzola, A. Sbarbati, F. Boschi, Multispectral Cerenkov luminescence tomography for small animal optical imaging, Optics Express 19 (13) (2011) 12605–12618.

[15] H. Liu, G. Ren, Z. Miao, X. Zhang, X. Tang, P. Han, S. Gambhir, Z. Cheng, Molecular optical imaging with radioactive probes, PloS one 5 (3) (2010) e9470.

[16] B. Beattie, D. Thorek, C. Schmidtlein, K. Pentlow, J. Humm, A. Hielscher, Quantitative modeling of Cerenkov light production efficiency from medical radionuclides, PloS one 7 (2) (2012) e31402.

[17] E. Ciarrocchi, N. Belcari, A. Del Guerra, S. Cherry, A. Lehnert, W. Hunter, W. McDougald, R. Miyaoka, P. Kinahan, Cherenkov luminescence measurements with digital silicon photomultipliers: a feasibility study, EJNMMI Physics 2 (1) (2015) 1.

[18] M. Shimamoto, K. Gotoh, K. Hasegawa, A. Kojima, Hybrid light imaging using Cerenkov luminescence and liquid scintillation for preclinical optical imaging in vivo, Molecular Imaging and Biology 18 (4) (2016) 500–509.

[19] M. King, C. Carpenter, C. Sun, X. Ma, Q. Le, J. Sunwoo, Z. Cheng, G. Pratx, L. Xing, β-Radioluminescence Imaging: A Comparative Evaluation with Cerenkov Luminescence Imaging, Journal of Nuclear Medicine 56 (9) (2015) 1458–1464.

[20] J. A. Thie, Understanding the standardized uptake value, its methods, and implications for usage, Journal of Nuclear Medicine 45 (9) (2004) 1431–1434.

[21] H. Everaert, C. Vanhove, T. Lahoutte, K. Muylle, V. Caveliers, A. Bossuyt, P. R. Franken, Optimal dose of 18F-FDG required for whole-body PET using an LSO PET camera, European Journal of Nuclear Medicine and Molecular Imaging 30 (12) (2003) 1615–1619.

[22] R. Gill, G. Mitchell, S. Cherry, Computed Cerenkov luminescence yields for radionuclides used in biology and medicine, Physics in Medicine and Biology 60 (11) (2015) 4263.

[23] A. Spinelli, M. Ferdeghini, C. Cavedon, E. Zivelonghi, R. Calandrino, A. Fenzi, A. Sbarbati, F. Boschi, First human Cerenkography, Journal of Biomedical Optics 18 (2) (2013) 020502–020502.

[24] D. Thorek, C. Riedl, J. Grimm, Clinical Cerenkov luminescence imaging of 18F-FDG, Journal of Nuclear Medicine 55 (1) (2014) 95–98.

[25] A. Spinelli, M. Pagliazzi, F. Boschi, Design of a multimodal fibers optic system for small animal optical imaging, Physica Medica: European Journal of Medical Physics 31 (1) (2015) 108–111.

[26] C. Mancini-Terracciano, R. Donnarumma, G. Bencivenga, V. Bocci, A. Cartoni, F. Collamati, I. Fratoddi, A. Giordano, L. Indovina, D. Maccora, et al., Feasibility of beta-particle radioguided surgery for a variety of nuclear medicine radionuclides, Physica Medica: European Journal of Medical Physics 43 (2017) 127–133.